arXiv:1606.04150v1 [astro-ph.EP] 13 Jun 2016

Photometric Measurements of H_2O Ice Crystallinity on Trans-Neptunian Objects *

Tsuyoshi Terai[1], Yoichi Itoh[2], Yumiko Oasa[3], Reiko Furusho[4], and Junichi Watanabe[4]

[1] *Subaru Telescope, National Astronomical Observatory of Japan, 650 North A'ohoku Place, Hilo, HI 96720, USA*

[2] *Center for Astronomy, University of Hyogo, 407-2 Nishigaichi, Sayo-cho, Sayo-gun, Hyogo 679-5313, Japan*

[3] *Faculty of Education, Saitama University, 255 Shimo-Okubo, Sakura, Saitama 338-8570, Japan*

[4] *National Astronomical Observatory of Japan, 2-21-1 Osawa, Mitaka, Tokyo 181-8588, Japan*

tsuyoshi.terai@nao.ac.jp

ABSTRACT

We present a measurement of H_2O ice crystallinity on the surface of trans-neptunian objects (TNOs) with near-infrared narrow-band imaging. The newly developed photometric technique allows us to efficiently determine the strength of an 1.65-μm absorption feature in crystalline H_2O ice. Our data for three large objects, Haumea, Quaoar, and Orcus, which are known to contain crystalline H_2O ice on the surfaces, show a reasonable result with high fractions of the crystalline phase. It can also be pointed out that if the H_2O-ice grain size is larger than $\sim$20 μm, the crystallinities of these objects are obviously below 1.0, which suggest the presence of the amorphous phase. Especially, Orcus exhibits a high abundance of amorphous H_2O ice compared to Haumea and Quaoar, possibly indicating a correlation between bulk density of the bodies and surface crystallization degree. We also found the presence of crystalline H_2O ice on Typhon and 2008 AP_{129}, both of which are smaller than the minimum size limit for inducing cryovolcanism as well as a transition from amorphous to crystalline through the thermal evolution due to the decay of long-lived isotopes.

Subject headings: Kuiper belt: general — planets and satellites: surfaces

1. INTRODUCTION

Trans-neptunian objects (TNOs) are believed to be ice-rich bodies formed in regions distant from the Sun. Several kinds of icy species have been detected from TNOs by previous visible and

*Based on data collected at Subaru Telescope, which is operated by the National Astronomical Observatory of Japan (NAOJ).

near-infrared spectroscopic observations. H_2O ice, known as the most abundant volatile material in the solar system, is generally the primary component on icy surfaces of TNOs except for the largest objects such as Pluto, Eris, Sedna, and Makemake, that are covered by CH_4 ice (e.g., Owen et al. 1993; Brown et al. 2005; Barucci et al. 2005; Licandro et al. 2006). H_2O ice is condensed from the vapor in nebula gas as amorphous phase in a cold environment far bellow 100 K, (Jenniskens et al. 1998; Mastrapa et al. 2008). Transition from amorphous to crystalline ice requires ∼1 hr at 130 K, while $\sim 10^3$ yr at 90 K (Jenniskens & Blake 1996). Pristine H_2O ice maintains an amorphous state from the beginning of the solar system if the temperature remains lower than ∼80 K. Although the typical surface temperature of TNOs is ∼40–60 K (Stansberry et al. 2008), the spectra of large TNOs obviously exhibit the absorption feature of crystalline H_2O ice at 1.65 μm, e.g., Charon (Brown & Calvin 2000; Buie & Grundy 2000), Quaoar (Jewitt & Luu 2004; Dalle Ore et al. 2009), Haumea (Barkume et al. 2006; Trujillo et al. 2007; Merlin et al. 2007), and Orcus (de Bergh et al. 2005; Barucci et al. 2008). Haumea's satellite Hi'iaka (Dumas et al. 2011) and collisional family members (Barkume et al. 2006) are also known to be covered by crystalline H_2O ice. Additionally, several moderate-size TNOs/Centaurs have been suggested to have surfaces covered in crystalline H_2O ice (e.g., Barucci et al. 2011).

These objects are highly likely to have experienced a certain process resulting in the production and/or provision of crystalline H_2O ice on their surfaces. Several mechanisms have been suggested, including radiogenic heating (Merk & Prialnik 2006; Guilbert-Lepoutre et al. 2011), cryovolcanism (Cook et al. 2007; Desch et al. 2009), and micrometeorite impact annealing (Porter et al. 2010). However, it remains unknown which of them primarily causes the presence of crystalline H_2O ice on the surfaces. Elucidation of the generation process could provide an insight into the formation, evolution, and possibly interior structure of icy small bodies in the outer solar system. For this purpose, it is essential to clarify the following ambiguous questions; (i) Is the presence of crystalline H_2O ice on the surfaces ubiquitous among TNOs? If yes, is the crystallinity constant among them? (ii) Does the presence/abundance of crystalline ice depend on the body size and/or other parameters? In the former case, what is the size limit for the surface containing crystalline ice?

In the present circumstances, however, the general knowledge regarding abundance distribution of surface crystallinity in the TNO population is still poor because of a lack of observational constraints. Most of the known TNOs are too faint to obtain spectra with sufficient quality to accurately determine the ratio of crystalline and amorphous phases on their surfaces even by largest-class telescopes.

In this paper, we introduce a new measurement technique for H_2O ice crystallinity on icy small bodies with near-infrared photometric data acquired by the Subaru telescope. We use the narrow-band filter called "NB1657", allowing us to evaluate the strength of 1.65-μm absorption of crystalline H_2O with high precision. The results demonstrate that this method is useful for an effective survey of the crystalline ice abundance from a large number of TNOs.

2. OBSERVATIONS AND DATA REDUCTION

Our observation was carried out on April 7, 2013, with Multi-Object InfraRed Camera and Spectrograph (MOIRCS; Ichikawa et al. 2006; Suzuki et al. 2008) mounted on the 8.2-m Subaru telescope. MOIRCS consists of two 2048×2048 arrays with pixel scale of 0.″117, each of which covers a $4' \times 3.'5$ field of view. We performed a near-infrared imaging using the H band and narrow band filter NB1657. The NB1657 with the center wavelength of 1.657 μm and band width of 0.019 μm (Koyama et al. 2014) is suitable for diagnosing the absorption of crystalline H_2O ice at 1.65 μm (see Figure 1). The sky condition was photometric, with a seeing size of mostly 0.″6–0.″8.

Our target objects consist of seven TNOs listed in Table 1. These objects have been reported to contain H_2O ice on the surfaces in the near-infrared spectroscopy by Brown et al. (2012), i.e., $f_{H_2O} \gtrsim 0.1$, where f_{H_2O} represents the spectral fraction of H_2O ice. The observational circumstances are shown in Table 2. Every image was taken with an exposure of 42–80 sec in the H band and 90–180 sec in the NB1657 under sidereal tracking. The sky motion within the exposure time is sufficiently smaller than the seeing size to treat the target objects as a point source. The NB1657 data was obtained between just before/after H-band imagings to reduce color uncertainty caused by rotational brightness variation.

Data reduction was conducted using IRAF produced by the National Optical Astronomy Observatories (NOAO) and MCSRED[1] (Tanaka et al. 2011) with standard processes: linearity correction, flat-fielding, sky subtraction, and distortion correction. Images with each band were shifted according to the sky motion of a target object and were combined. Position-matched composite images were also created for determining the point spread function (PSF) from the field stars. We adopted aperture photometry for flux measurement using the IRAF/APPHOT package. To increase signal-to-noise ratio, the aperture correction technique has been applied. Summed pixel counts within a small aperture with radius of ∼0.5–0.8 arcsec were converted into total flux based on the flux ratio computed from the PSF profile given by the field stars. Haumea is an exception because of a lack of field stars and thus its flux was directly measured with a large aperture (2.2 arcsec in radius). The H-band magnitude and $H-$NB1657 index were calibrated with a G2V star, 2MASS J06430376−0117471 ($H = 13.630 \pm 0.031$ mag) or 2MASS J16375427+4052592 ($H = 13.161 \pm 0.027$ mag), taken within 2.5 hours of target data acquisition. $\Delta(H-\text{NB1657})$ is defined as the offset $H-$NB1657 index that the Sun color is subtracted.

The results of photometry are shown in Table 3. Most of the $H-$NB1657 indexes have been determined with uncertainty of ∼0.02 mag or less, allowing us to estimate abundance of crystalline H_2O ice on the surface of the target objects. Unfortunately, however, Ceto contains a large photometric error because of the insufficient exposure time (500 sec with the H and 720 sec with the NB1657 filters) due to restriction of the observation time. We exclude Ceto from the sample for the following analysis.

[1] http://www.naoj.org/staff/ichi/MCSRED/mcsred.html

3. RESULTS

3.1. Model Spectra

From the measured $H-$NB1657 index, we obtain a fraction of the crystalline phase in the H_2O ice spectrum, hereinafter called the "crystallinity factor" ($f_{\rm crys}$). In this paper, the reflectance spectrum of phase-mixed H_2O ice, $S_{H_2O}(\lambda)$ (λ is wavelength in μm), is represented by a linear sum of the crystalline and amorphous spectra ($S_{\rm crys}(\lambda)$ and $S_{\rm amor}(\lambda)$, respectively) as defined in Newman et al. (2008), i.e.,

$$S_{H_2O}(\lambda) = f_{\rm crys}\, S_{\rm crys}(\lambda) + (1 - f_{\rm crys})\, S_{\rm amor}(\lambda). \quad (1)$$

Modeling reflectance spectra of the target objects is required to convert the 1.65-μm absorption strength derived from $\Delta(H-{\rm NB1657})$ into the crystallinity factor.

We assume that near-infrared spectra of those bodies are represented by a simple model consisting of H_2O ice spectrum and linear continuum presented by Brown et al. (2012). The model spectrum, $S(\lambda)$, is given as

$$S(\lambda) = f_{H_2O}\, S_{H_2O}(\lambda) + (1 - f_{H_2O})\, [m_{\rm cont}(\lambda - 1.74\,\mu{\rm m}) + 0.49]\,, \quad (2)$$

where f_{H_2O} is a spectral fraction of H_2O ice and $m_{\rm cont}$ is a continuum slope. The H_2O ice spectra were generated from the geometric albedo A_p described by the radiative transfer model of Hapke (1993) as

$$A_p \simeq r_0 \left(\frac{1}{2} + \frac{1}{6} r_0\right) + \frac{w}{8}\,[(1 + B_0)p(0) - 1]\,, \quad (3)$$

where w is the single scattering albedo given from the optical constants and grain size, r_0 is the diffusive reflectance given by $\frac{1-\sqrt{1-w}}{1+\sqrt{1-w}}$, B_0 is the total amplitude of the opposition surge, and $p(0)$ is the phase function at zero phase angle. We used $B_0 = 0.67$, the typical value among icy satellites (Verbiscer & Helfenstein 1998) as in Merlin et al. (2009), and isotopic scattering, i.e., $p(0) = 1.0$. The optical constants of amorphous and crystalline H_2O ices were derived from the laboratory data provided by Mastrapa et al. (2008)[2].

The grain size is one of the most sensitive parameters to determine the reflectance spectrum but still unknown. We tentatively used uniform grain particles with a diameter of $d = 50$ μm as in Brown et al. (2012). The uncertainty due to the dependency on grain size is discussed in Section 3.3.

The absorption spectrum of H_2O ice, especially the 1.56-μm and 1.65-μm bands in crystalline H_2O ice, varies with temperature (e.g., Grundy & Schmitt 1998). Surface temperature of airless solid bodies depends on the solar flux, rotation, and surface properties. Stansberry et al. (2008)

[2]Mastrapa, R. M. E., Optical Constants and Lab Spectra of Water Ice V1.1. EAR-X-I1083-5-ICESPEC-V1.1. NASA Planetary Data System, 2012 (`http://sbn.psi.edu/pds/resource/icespec.html`).

presented temperatures of 49 TNOs/Centaurs derived from 24-μm and 70-μm flux data collected by the Spitzer Space Telescope. Figure 2 shows the color temperatures as a function of target distance from the Sun at the observations. The plot is well approximated by an equation of

$$T = (389 \pm 14) r_{\rm h}^{-1/2} + (-7.1 \pm 3.3), \tag{4}$$

where T and $r_{\rm h}$ are the temperature in kelvin and heliocentric distance in au, respectively. Here, we consider the thermal temperatures derived from this equation assuming isothermal blackbodies as their ice temperatures. Its appropriateness is assessed below. Mastrapa's dataset contains the optical constants of crystalline H_2O ice at temperatures from 20–150 K every 10 K and those of amorphous H_2O ice at temperatures higher/lower than 70 K. Based on the estimated temperatures, we drew the spectral reflectance of crystalline/amorphous ices from the optimum optical constant data for each target object as seen in Table 4. The model spectra of the target objects were generated from Equation (2) with the synthetic spectra of H_2O ice as mixtures of crystalline and amorphous phases given by Equation (1).

The spectral fraction of H_2O ice f_{H_2O} and continuum slope $m_{\rm cont}$ were assumed to be those suggested by Brown et al. (2012) as listed in Table 1. Note that these parameters have been estimated from simple modeling with the optical constants of fully crystallized ice. We evaluated the variability of f_{H_2O} determined through the model depending on crystallinity. The synthetic spectra from Equation (2) were compared between pure crystalline ice and amorphous-dominated/mixed ones by least-squares optimization under the same conditions as Brown et al. (2012), i.e., temperatures of 50 K, grain size of 50 μm, and wavelength ranges of 1.45–1.80 μm and 1.95–2.30 μm. Table 5 shows the best-fit f_{H_2O} values for the spectra created with $f_{\rm crys}$ of 0.00, 0.25, and 0.50. Since there are only small differences from the given values in any $f_{\rm crys}$ cases, one can see that f_{H_2O} has little dependency on crystallinity. It indicates the validity of our crystallinity measurement based on the published f_{H_2O} values.

To compare with the photometric data, the model spectra were converted into $\Delta(H-{\rm NB1657})$ by

$$\Delta(H - {\rm NB1657}) = 2.5 \log \left[\frac{\int R_{\rm NB}(\lambda) S(\lambda) \lambda F_{\lambda,\odot}(\lambda) d\lambda \; / \int R_H(\lambda) S(\lambda) \lambda F_{\lambda,\odot}(\lambda) d\lambda}{\int R_{\rm NB}(\lambda) \lambda F_{\lambda,\odot}(\lambda) d\lambda \; / \int R_H(\lambda) \lambda F_{\lambda,\odot}(\lambda) d\lambda} \right], \tag{5}$$

where $R_H(\lambda)$ and $R_{\rm NB}(\lambda)$ are the response functions for the H and NB1657 bands, respectively. $F_{\lambda,\odot}(\lambda)$ is the wavelength flux density of the Sun. The response functions include atmospheric transmission at the summit of Maunakea generated by ATRAN modelling software (Lord 1992) assuming airmass of 1.0 and water vapor column of 1.0 mm. We used the solar reference spectrum distributed by STScI Calibration Database System[3].

[3] http://www.stsci.edu/hst/observatory/crds/calspec.html

3.2. Crystallinity

By comparing the obtained $\Delta(H-\mathrm{NB1657})$ index with the model spectra, we determined the crystallinity factors of H_2O ice for each target object. Figure 3 shows $\Delta(H-\mathrm{NB1657})$ derived from our observation and modeling with respect to the crystallinity factor. The point where the model curve intersects with the measured value represents a plausible crystallinity factor. The resulting crystallinity factors are listed in Table 4. The determination accuracy depends on photometric precision and the slope of the model curve given by abundance of H_2O ice. For bright objects including Orcus, Haumea, and Quaoar, the crystallinity factor has been fixed with accuracy of $\sim$0.1. Huya is also bright, however, the error is very large due to low $f_{\mathrm{H_2O}}$ (0.08 ± 0.02) causing a little $\Delta(H-\mathrm{NB1657})$ variation with crystallinity factor. This implies that $f_{\mathrm{H_2O}} \sim 0.1$ is the limit of application of this technique for TNOs in Subaru/MOIRCS observation.

Under hypothetical ice conditions with temperature based on thermal flux and grain size of 50 μm, the model matching indicates abundant crystalline H_2O ice on the surfaces of Haumea and Quaoar, as well as a moderate amount of the crystalline phase on Orcus. This result agrees with the previous spectroscopic works showing a significant feature of the 1.65 μm absorption on those objects (e.g., de Bergh et al. 2005; Trujillo et al. 2007; Jewitt & Luu 2004). Typhon also shows high crystallinity, consistent with the spectral model presented by Guilbert et al. (2009) (5% of crystalline and 0% of amorphous).

We evaluated the validity of this technique through comparison with published near-infrared spectra of Haumea and Quaoar obtained with Keck/NIRC[4] (Barkume et al. 2008). Figure 4 shows those spectra as well as the spectral models generated from Equation (2) with the crystallinities measured by this work. The models well reproduce the observed spectra inclusive of the 1.65-μm feature in both objects. It supports that our photometric method is useful to constrain the phase ratio of crystalline to amorphous for an icy small body of which $f_{\mathrm{H_2O}}$ is known. The effect of the assumed ice properties, temperature and grain size, for determination of the crystallinity factor is examined in the following section.

3.3. Ice Temperature And Grain Size

The depth and center wavelength of the 1.65-μm band sensitively vary with temperature and grain size (Fink & Larson 1975; Clark 1981; Grundy & Schmitt 1998; Taffin et al. 2012), while the two parameters were given as thermal temperature estimated from Equation (4) and $d = 50$ μm, respectively, in the above modeling. Grundy et al. (1999) presented disk-averaged H_2O ice temperatures of Jovian, Saturnian, and Uranian satellites derived from their near-infrared spectra. They pointed out that the ice temperature is generally lower than the brightness

[4] `http://web.gps.caltech.edu/$^\sim$pa/data/kbo_info.html`

temperature derived from thermal emission which is sensitive to warm regions on the surface with the typical difference of ∼10 K. The target objects could actually have a lower surface temperature.

We conducted additional modeling with the same processes presented in Section 3.1 but using the optical constant data of crystalline H_2O ice at temperatures 10 K lower than those in Table 4. The results, shown in Table 6, indicate no significant change in the obtained crystallinity factor compared with the original spectrum model in any objects. Such a difference in the given temperature causes a systematic error of no more than ∼10% for our crystallinity measurements.

On the other hand, grain size can induce considerable uncertainty in the modeling. Although the dominant size of the ice grains on surface layer of TNOs is still unknown, Barucci et al. (2011) reported surface composition models of 12 TNOs/Centaurs based on their near-infrared spectroscopy data showing that most of their surfaces contain H_2O ice (in crystalline and/or amorphous states) with the particle diameter of ∼10–200 μm. Many of the previous studies of TNO/Centaur spectra showed the best-matched grain sizes in this range. Note that H_2O ice with larger ice grains enhance the absorption coefficients, but the enhancement saturates at the diameter of ∼1000 μm. In contrast, if the grains are smaller than ∼10 μm, the absorptions are too weak to measure the 1.65-μm feature via $\Delta(H-\mathrm{NB1657})$ index. Thus, our technique is applicable to objects whose surfaces are dominated by H_2O ice with the grain size of ∼10–1000 μm.

We examined the variation of crystallinity factor for our observed objects among the spectral models with grain sizes from 10 μm to 200 μm in diameter (see Figure 5). A uniform size between the crystalline and amorphous particles was assumed in each pattern. The results are shown in Figure 6. One can see that the crystallinity factor monotonically decreases with increasing grain size. This is because of the optical characteristic of H_2O ice that larger grains increase the amount of 1.65-μm absorption rather than that of entire absorption covered by the H band, as pointed out in Grundy & Schmitt (1998). Although the crystallinity factor varies greatly between the smallest and largest grain sizes, it remains larger than ∼0.5 within the error in Haumea, Quaoar, Typhon, and 2008 AP_{129}. Orcus has a slightly lower crystallinity in case of the largest grain sizes, but definitely contains a certain level of crystalline ice. This result indicates that all of the five objects whose crystallinity has been precisely determined are likely to be covered by a surface containing crystalline-dominant H_2O ice or comparable to it.

3.4. Impurities

The spectrum model given by Equation (2) approximates the surface reflectance spectrum of the target objects as a combination of H_2O ice and other materials of which the total spectrum shows a linear-sloped continuum with no absorption feature. For the H-band data, this assumption seems to be reasonable because most non-H_2O ices which are potentially contained on the TNOs' surface, e.g., CH_3OH, CO, CO_2, N_2, and NH_3, have no or only slight absorptions over the wavelength range (Gerakines et al. 2005; Cruikshank et al. 1984). However, CH_4 ice could be influential for

determination of H_2O ice crystallinity because it exhibits several absorption features from 1.5 μm to 1.8 μm (Pearl et al. 1991). In particular, the strong absorption bands at 1.67 μm possibly makes a significant negative contribution to the $\Delta(H-\mathrm{NB1657})$ index.

Various near-infrared spectroscopies suggest the presence of CH_4 ice on several TNOs with H_2O ice-rich surface including Quaoar (Schaller & Brown 2007; Dalle Ore et al. 2009) and Orcus (Barucci et al. 2008; Delsanti et al. 2010; Carry et al. 2011). According to previous studies of the two spectra, the average fraction of CH_4 ice is $\sim$0.05, corresponding to $CH_4/H_2O \sim 0.15$. To evaluate the effect of CH_4 ice mixing on measurements of H_2O ice crystallinity, we calculated the $\Delta(H-\mathrm{NB1657})$ index with several patterns of the particle number ratio (CH_4/H_2O = 0.05–0.20) and CH_4 ice grain size (d = 10, 50, and 100 μm). The optical constants of CH_4 ice used for the spectrum modeling are as follows: (i) the real part of refractive index n is given by $n = 1.38 - 0.03\lambda$ (0.67 $\mu\mathrm{m} \leq \lambda \leq$ 2.0 μm; de Bergh et al. 2008), (ii) the imaginary part of refractive index k is converted from the absorption coefficients of phase I CH_4 ice (stable between 20 K and 90 K) presented by Grundy et al. (2002). The synthetic model spectra were generated from Equation (2) by replacing the reflectance spectrum of H_2O ice, S_{H_2O}, with that of mixed ices of H_2O and CH_4 derived from the intimate mixture model developed by Hapke (1993). The grain size of H_2O ice was fixed to d = 50 μm.

The results are shown in Figure 7. If CH_4 ice grain is equal to or smaller than H_2O ice grain, the H_2O ice crystallinity factors are larger than 0.50 and 0.25 for Quaoar and Orcus, respectively. The situation is similar if $CH_4/H_2O \lesssim 0.05$. In contrast, the absorption due to the larger-grain CH_4 ice on the surface with $CH_4/H_2O \gtrsim 0.1$ dominates at $\sim$1.65 μm and could cause a great uncertainty of H_2O ice crystallinity.

We recognize that Dalle Ore et al. (2009) and Carry et al. (2011) provide the most reliable spectral modeling for Quaoar and Orcus, respectively, among the published works. The former suggests Quaoar's surface containing fine CH_4 ice grains of $d \sim 10$ μm with a slightly high fraction of $CH_4/H_2O \sim 0.3$. The latter suggests Orcus's surface containing coarse CH_4 ice grains of $d \sim 100$ μm with a tiny fraction of $CH_4/H_2O < 0.03$. If those parameters are simply applied to our modeling, they indicate that the potential presence of CH_4 ice is unlikely to induce significant overestimation of H_2O ice crystallinity against Quaoar and Orcus.

4. DISCUSSION

Provided that the observed objects are coated by H_2O ice grain of $d \lesssim 50$ μm with negligible contamination by other ices such as CH_4, our results suggest the following implications:

(i) Not only Haumea and Quaoar known as large objects rich in crystalline H_2O ice, but also smaller objects, Typhon and 2008 AP_{129}, contain crystalline-dominated H_2O ice on the surfaces.

(ii) Orcus has a crystallinity of comparable to 0.5, obviously lower than Haumea and Quaoar.

(iii) No objects with low-crystallinity surface have been found in our well-measured TNO sample.

The initial state of H_2O ice in TNOs is likely to be amorphous if the bodies formed beyond ∼25 au from the Sun (Kawakita et al. 2006). Such pristine ice could be heated and crystallized through thermal evolution after the formation. Based on the timescale to onset of crystallization (Jenniskens & Blake 1996) and the timescale to completion of crystallization (Kouchi et al. 1994), amorphous ice at > 70 K would be crystallized within the solar system age (Mastrapa et al. 2013). Additionally, surface annealing due to micrometeorite impacts may also be effective in inducing ice crystallization. In this section, we discuss several possible mechanisms for crystallization of the surface H_2O ice of TNOs.

Note that crystalline H_2O ice can be amorphized by irradiation of UV photon as well as energetic particles such as protons and electrons from the solar wind and cosmic rays. Leto & Baratta (2003) and Leto et al. (2005) confirmed that UV photolysis induces the amorphization at 16 and 90 K, respectively, through irradiation experiments. However, as Hudson et al. (2008) pointed out, the UV penetration depth is much less than the optical depth in near-infrared (∼350 μm). The effect of UV photolysis can be excluded in this observation. On the other hand, protons above ∼1 MeV and electrons above ∼0.1 MeV have stopping ranges larger than the optical depth for H_2O ice target (Hudson et al. 2008). Mastrapa & Brown (2006) presented the results of proton irradiation experiments, indicating (i) amorphous ice was produced at low temperatures (< 40 K), (ii) some crystalline ice persisted at 50 K after irradiation, and (iii) the crystalline spectrum showed only slight changes at ≥ 70 K.

Zheng et al. (2009) investigated the effect of electron irradiation on the near-infrared spectra and found that crystalline H_2O ice can be converted only partially to amorphous at 40 K or higher. According to measurements from the Geostationary Operational Environmental Satellites (GOES)[5], the fluence ratio of electrons to protons above 1 MeV from solar wind is 10^3–10^4. The interplanetary flux of proton from cosmic ray is $\sim 10^2$ greater than that from solar wind above 1 MeV at heliocentric distance of 40 au (Cooper et al. 2003). Thus, the electron is likely to be the dominant component of energetic particle irradiance on surfaces of icy bodies in the main trans-neptunian region. Although there are a lot of discrepancies among previous experimental studies as mentioned in Mastrapa et al. (2013), assuming the irradiation tolerance of crystalline H_2O ice based on the experimental results of Zheng et al. (2009), the amorphization process could be only limited. Here we ignore the effect of radiation-induced amorphization in the following discussion.

[5]The data distributed by NOAA/National Centers for Environmental Information (`ftp.ngdc.noaa.gov`).

4.1. Insolation

Prior to discussions of the thermal evolution, we should confirm the variations in surface temperature of the target objects over an orbit. Amorphous ice would be crystallized on surfaces that have been much warmer than 70 K over the timescale of the solar system age or less (Jenniskens & Blake 1996; Kouchi et al. 1994). Even if there is no heat source except solar insolation, the transition from amorphous to crystalline occurs on the surface of bodies sufficiently close to the Sun. All the target objects other than Typhon have perihelion distances larger than 28.5 au, which are converted into surface temperature less than 66 K by Equation (4). Assuming no experiences of significant migration from the formation, their surfaces have been cold enough for amorphous ice to be continuously stable.

However, Typhon has a high orbital eccentricity (0.54) allowing it to approach up to 17.5 au to the Sun. Around its perihelion, the sunward surface would be warmed up to ∼86 K, while the ordinary temperature is ∼50 K during most of the orbit. In the model of Jenniskens & Blake (1996), the time to onset of crystallization at the temperature is $\sim 10^6$ yr. The insolation heating can induce surface crystallization if Typhon keeps such an eccentric orbit over the age of the solar system and the intermittent contribution has monotonically accumulated.

4.2. Radiogenic Heating

The decay of radioactive isotopes contained in dust mixed with ice is the most important heat source for the internal thermal evolution of small icy bodies in the outer solar system. It allows the crystallization to proceed outward from the deep interior of the body.

In Prialnik & Podolak (1995), thermal evolutionary calculations of icy bodies larger than 40 km in diameter (D) with heat sources of ^{26}Al and four long-lived radioactive isotopes indicate that H_2O ice on the outer layer seems to be left in the amorphous form. Choi et al. (2002) also reported that ^{26}Al decay could not raise the surface temperature of TNOs with D = 20–1000 km higher than ∼50 K and not induce H_2O ice crystallization at the surface layers. Those models cannot explain surface crystallization of objects with $D > 100$ km.

However, assuming that the objects were formed closer to the Sun than the present orbits, radiogenic heating can potentially crystallize the surface ice because of fast accretional growth, thus sufficient radiogenic heating by ^{26}Al. The simulations of Merk & Prialnik (2006) showed that icy bodies above $D \sim 30$ km originally located around 20 au could be covered by a crystalline ice surface. McKinnon et al. (2008) showed that if icy bodies formed at heliocentric distance less than ∼32 au, the crystalline/amorphous ice boundary reaches the surface.

More recent work by Guilbert-Lepoutre et al. (2011) presented three-dimensional simulations to compute the thermal evolution of icy small bodies with heat sources of several short- and long-lived radioactive isotopes. Their results suggest:

- When the growth advanced quickly (∼1 Myr) and short-lived isotope decay effectively contributes to the thermal evolution, objects with $D > 100$ km retain only a thin (< 2 km) layer of amorphous H_2O ice on their surface, that may possibly be removed by impact excavating. In addition, provided such objects are formed close enough to the Sun (10–15 au), crystallization would be triggered at the surface by insolation.

- When the thermal evolution is dominated by long-lived isotope decay, only large objects ($D > 600$ km) with a bulk density of at least 1500 kg m^{-3} should contain crystalline H_2O ice close to the surface.

Our findings regarding the presence of crystalline H_2O ice on Typhon and 2008 AP_{129} agree with the first scenario. In contrast, Typhon and possibly 2008 AP_{129} (see Table 1) are inconsistent with the second one. Based on the model of Guilbert-Lepoutre et al. (2011), at least those small objects should have grown in a sufficiently short time scale for the surfaces to be heated up to the crystallization temperature by the decay of short-lived isotopes unless they were formed close to the Sun (10–15 au).

Such a rapid formation as to induce a sufficient heating for surface ice crystallization due to the decay of short-lived isotopes also can occur at a smaller heliocentric distance than the current location. Actually, several theoretical studies support this model. Weidenschilling (2004) presented coagulation simulations of planetesimal growth in the outer solar system and showed the formation of objects with $D > 100$ km only inside ∼30 au. More recently, Kenyon & Bromley (2012) performed N-body coagulation calculations for the formation and evolution of TNOs, indicating that objects at 15–18 au grow up to 100 km in diameter within ∼1 Myr at earliest, while it takes more than 10 Myr at 33–40 au. Outward transport of planetesimals from the inner regions via the planetary migration has been believed to take place based on numerical simulations for dynamical evolutions of giant planets and TNOs (e.g., Gomes 2003; Levison & Morbidelli 2003; Hahn & Malhotra 2005; Levison et al. 2008). The rapid growth around 20 au from the Sun is a plausible mechanism for crystallization of surface ice from the early radioactive heating on TNOs as small as Typhon.

The thermal evolution model may also be able to explain the low fraction of crystalline ice on Orcus compared with Haumea and Quaoar. One of the important parameters that the heating rate depends on is bulk density of the body. A higher density increases the abundance of dust materials containing radioactive isotopes and thus enhances heating efficiency. The difference in bulk density possibly causes the variation in crystallinity among comparable-size objects. Guilbert-Lepoutre et al. (2011) suggest that a density of at least 1.5 g cm^{-3} is required for the presence of crystalline ice on the surface of objects with $D \gtrsim 600$ km. Haumea is well known to have a high density (∼ 2.6 g cm^3; Rabinowitz et al. 2006; Lacerda & Jewitt 2007). Quaoar's density also has been estimated to be high as $2.18^{+0.43}_{-0.36}$ g cm^{-3} from thermal flux (Fornasier et al. 2013) or 1.99 ± 0.46 g cm^{-3} from occultation (Braga-Ribas et al. 2013). In contrast, Orcus exhibits an obviously lower density of ∼1.5 g cm^{-3} (Brown et al. 2010), just about the same value as the

criteria for surface ice crystallization shown by Guilbert-Lepoutre et al. (2011). This fact suggests the possibility that Orcus failed to take a sufficient rise in temperature of the upper layer for crystallizing most of the surface H_2O ice due to a deficiency in the amount of radioactive isotopes. The potential correlation between crystallinity and bulk density could support the hypothesis that radiogenic heating is the dominant effect on surface crystallization for TNOs.

4.3. Cryovolcanism

A portion of surface ice may not have been formed in-situ but been supplied through the interior by geological activity of ice volcanic eruption, so-called cryovolcanism. Actually, atmospheric plumes have been shown on several icy satellites of giant planets, such as Triton (Smith et al. 1989; Kargel 1994), Enceladus (Porco et al. 2006; Spencer et al. 2009), and Europa (Roth et al. 2014), as possible evidence of cryovolcanic events. The occurrence of substantial liquid H_2O flow to the surface requires some sort of continual heating process to melt the subsurface ice. For the satellites, tidal energy dissipation is likely to be a major heat source (e.g., Ruiz & Tejero 2000). Even though inclusion of NH_3 in H_2O ice allows the melting point to drop from 273 K to 176 K at minimum (Kargel et al. 1991) and decreases the thermal conductivity, it is still uncertain whether the cryovolcanic activity can be driven on TNOs primarily by long-lived radioactive isotopes without tidal heating.

Cook et al. (2007) suggested that a body with $D > 1200$ km composed of rock with a mass fraction $\gtrsim 0.7$ (corresponding to a bulk density $\gtrsim 1.8$ g cm^{-3}) and NH_3-rich H_2O ice ($\sim$0.15 by weight) could develop cryovolcanism and be steadily resurfaced by crystalline H_2O ice with a sufficient rate to be detected by near-infrared wavelength. Haumea, with a mean diameter of 1200–1300 km (Lellouch et al. 2010; Fornasier et al. 2013) and a density of 2.6 g cm^{-3} (Lockwood et al. 2014), satisfies those conditions. Quaoar is slightly smaller than the criteria size ($\sim$1000–1100 km) and has a high density (1.99 ± 0.46 g cm^{-3}; Braga-Ribas et al. 2013, $2.18^{+0.43}_{-0.36}$ g cm^{-3}; Fornasier et al. 2013). Orcus is likely to be comparable in size to Quaoar ($\sim$850–950 km; Brown et al. 2010; Lim et al. 2010; Fornasier et al. 2013), while the density is relatively low ($1.53^{+0.15}_{-0.13}$ g cm^{-3}; Fornasier et al. 2013). As pointed out by Desch et al. (2009), the ice containing CH_3OH along with NH_3 freezes at lower temperature (153 K; Kargel 1994) and therefore is likely to reduce the minimum diameter of a TNO which can retain liquid H_2O to 800–1000 km. Cryovolcanism may be active on Quaoar and Orcus if they consist of CH_3OH-NH_3-H_2O ice.

Unfortunately, our results cannot provide explicit constraints on the source of crystalline H_2O ice at the surfaces of Haumea, Quaoar, and Orcus. On the other hand, Typhon and 2008 AP_{129} are likely to be too small to exhibit cryovolcanic activity even if antifreeze compounds such as NH_3 and CH_3OH are sufficiently mixed in the subsurface ice.

4.4. Other mechanisms

Instead of the internal heat sources as mentioned above, H_2O ice crystallization on surfaces of airless bodies in the trans-neptunian region could be induced by impacts of meteorites such as interplanetary dust particles (IDPs). Cook et al. (2007) assessed possible mechanisms with micrometeorites for explaining the presence of crystalline H_2O ice on Charon's surface, namely, impact gardening and annealing. They approximated the mass flux of IDPs from Pioneer 10 observations as 2.4×10^{-17} kg s^{-1} m^{-2} at 18 au and concluded that those mechanisms make little contribution to surface renewal on either Charon or other TNOs. In contrast, Porter et al. (2010) expected the IDP flux at Uranus to be 1.2×10^{-16} kg s^{-1} m^{-2} and claimed that the impact annealing could be effective for surface crystallization on TNOs.

As seen in Table 2 of Porter et al. (2010), the impact velocity of IDPs and required dust flux for annealing are similar among objects in the main trans-neptunian belt. Assuming homogeneous IDP distribution over the region, surface crystallinity would be almost uniform among TNOs if micrometeorite impacts are the primary factor. However, considering our result indicating a low crystallinity of Orcus compared with Haumea and Quaoar, micrometeorite annealing seems not to be a major mechanism of surface crystallization at least for icy objects as large as Orcus.

Finally, we focus on the unique situation of 2008 AP_{129} that has an orbit consistent with the Haumea collisional family (Brown et al. 2007). The relative velocity to the estimated collision's center of mass, $\sim$140 m s^{-1}, also agrees with the velocity dispersion of the known family members (50–300 m s^{-1}), suggesting a dynamical association with the Haumea family (Volk & Malhotra 2012). The spectra of family members uniquely show significantly high fractions of H_2O ice as well as the crystalline feature (Barkume et al. 2008; Barucci et al. 2011; Brown et al. 2012). However, 2008 AP_{129} contains only a minor fraction of H_2O ice ($f_{H_2O} = 0.14 \pm 0.09$; Brown et al. 2012), which prevents characterization of the membership. If 2008 AP_{129} originates from a collisional fragment as an ice-poor family member, the presence of crystalline H_2O ice on the surface is natural because the body is likely to derive from the icy mantle of Haumea. The lack of ice could be explained from inhomogeneous compositions of the partial differentiation (Volk & Malhotra 2012) although the actuality is still unknown.

5. CONCLUSIONS

We develop a new technique for measuring the crystallinity of H_2O ice on the surface of TNOs with near-infrared narrow-band photometry using Subaru/MOIRCS. The strength of the 1.65-μm absorption band for five objects has been obtained and converted into the fraction of crystalline ice by comparing with the spectrum model. The largest objects, Haumea, Quaoar, and Orcus, show a crystalline-rich icy surface as many previous spectroscopic studies have reported, while it is also found out that their surfaces are likely to contain amorphous ice unless the grain size is smaller than $\sim$20 μm. For Haumea and Quaoar, the model spectra based on the determined fractions of

crystalline ice well agree with the published near-infrared spectra, indicating reasonable accuracy of our measurements.

The results indicate that H_2O ice on Haumea and Quaoar are highly dominated by the crystalline state, while Orcus shows a higher fraction of amorphous ice. Based on the model of thermal evolution due to radiative decay, the low bulk density of Orcus could cause suppression of the surface heating and stagnation in crystallization. It is of great significance to examine the possibility of the positive correlation between bulk density of the body, i.e., abundance of refractory inclusion, and surface crystallinity, providing a critical clue for understanding the crystallization mechanism.

We also found the presence of crystalline H_2O ice on Typhon and 2008 AP_{129}. Those objects are smaller than the expected critical size ($D \sim 600$ km) for surface crystallization assuming that they were formed far enough from the Sun (> 15 au) and the initial thermal evolution was dominated by the decay of long-lived isotopes Guilbert-Lepoutre et al. (2011). It is still uncertain which thermal or non-thermal process is the primary crystallization mechanism for midsize TNOs. Further investigations are required to determine whether the body size affects the production of crystalline H_2O ice at the surface layer.

We are grateful to Tadayuki Kodama who kindly provided the NB1657 filter to open-use observers. We thank Ichi Tanaka for technically supporting our observation and data reduction, as well as Naruhisa Takato for fruitful comments on the manuscript. We also thank an anonymous referee for helpful comments and suggestions. This study is based on data collected at Subaru Telescope, National Astronomical Observatory of Japan.

REFERENCES

Barkume, K. M., Brown, M. E., & Schaller, E. L. 2006, ApJ, 640, L87

Barkume, K. M., Brown, M. E., & Schaller, E. L. 2008, AJ, 135, 55

Barucci, M. A., Cruikshank, D. P., Dotto, E., et al. 2005, A&A, 439, L1

Barucci, M. A., Merlin, F., Guilbert, A., et al. 2008, A&A, 479, L13

Barucci, M. A., Alvarez-Candal, A., Merlin, F., et al. 2011, Icarus, 214, 297

Braga-Ribas, F., Sicardy, B., Ortiz, J. L., et al. 2013, ApJ, 773, 26

Brown, M. E., & Calvin, W. M. 2000, Science, 287, 107

Brown, M. E., Trujillo, C. A., & Rabinowitz, D. L. 2005, ApJ, 635, L97

Brown, M. E., Barkume, K. M., Ragozzine, D., & Schaller, E. L. 2007, Nature, 446, 294

Brown, M. E., Ragozzine, D., Stansberry, J., & Fraser, W. C. 2010, AJ, 139, 2700

Brown, M. E., Schaller, E. L., & Fraser, W. C. 2012, AJ, 143, 146

Buie, M. W., & Grundy, W. M. 2000, Icarus, 148, 324

Carry, B., Hestroffer, D., DeMeo, F. E., et al. 2011, A&A, 534, AA115

Choi, Y.-J., Cohen, M., Merk, R., & Prialnik, D. 2002, Icarus, 160, 300

Clark, R. N. 1981, J. Geophys. Res., 86, 3087

Cook, J. C., Desch, S. J., Roush, T. L., Trujillo, C. A., & Geballe, T. R. 2007, ApJ, 663, 1406

Cooper, J. F., Christian, E. R., Richardson, J. D., & Wang, C. 2003, Earth Moon and Planets, 92, 261

Cruikshank, D. P., Brown, R. H., & Clark, R. N. 1984, Icarus, 58, 293

Dalle Ore, C. M., Barucci, M. A., Emery, J. P., et al. 2009, A&A, 501, 349

de Bergh, C., Delsanti, A., Tozzi, G. P., et al. 2005, A&A, 437, 1115

de Bergh, C., Schmitt, B., Moroz, L. V., Quirico, E., & Cruikshank, D. P. 2008, The Solar System Beyond Neptune, 483

Delsanti, A., Merlin, F., Guilbert-Lepoutre, A., et al. 2010, A&A, 520, AA40

Desch, S. J., Cook, J. C., Doggett, T. C., & Porter, S. B. 2009, Icarus, 202, 694

Dumas, C., Carry, B., Hestroffer, D., & Merlin, F. 2011, A&A, 528, A105

Fink, U., & Larson, H. P. 1975, Icarus, 24, 411

Fornasier, S., Lellouch, E., Müller, T., et al. 2013, A&A, 555, A15

Gerakines, P. A., Bray, J. J., Davis, A., & Richey, C. R. 2005, ApJ, 620, 1140

Gomes, R. S. 2003, Icarus, 161, 404

Grundy, W. M., & Schmitt, B. 1998, J. Geophys. Res., 103, 25809

Grundy, W. M., Buie, M. W., Stansberry, J. A., Spencer, J. R., & Schmitt, B. 1999, Icarus, 142, 536

Grundy, W. M., Schmitt, B., & Quirico, E. 2002, Icarus, 155, 486

Guilbert, A., Alvarez-Candal, A., Merlin, F., et al. 2009, Icarus, 201, 272

Guilbert-Lepoutre, A., Lasue, J., Federico, C., et al. 2011, A&A, 529, A71

Hahn, J. M., & Malhotra, R. 2005, AJ, 130, 2392

Hapke, B. 1993, Theory of reflectance and emittance spectroscopy (Topics in Remote Sensing; Cambridge: Cambridge Univ. Press)

Hudson, R. L., Palumbo, M. E., Strazzulla, G., et al. 2008, The Solar System Beyond Neptune, 507

Hudson, R. L., Gerakines, P. A., & Moore, M. H. 2014, Icarus, 243, 148

Ichikawa, T., Suzuki, R., Tokoku, C., et al. 2006, Proc. SPIE, 6269, 38

Jenniskens, P., & Blake, D. F. 1996, ApJ, 473, 1104

Jenniskens, P., Blake, D. F., & Kouchi, A. 1998, Solar System Ices, 227, 139

Jewitt, D. C., & Luu, J. 2004, Nature, 432, 731

Kargel, J. S., Croft, S. K., Lunine, J. I., & Lewis, J. S. 1991, Icarus, 89, 93

Kargel, J. S. 1994, Earth Moon and Planets, 67, 101

Kawakita, H., Ootsubo, T., Furusho, R., & Watanabe, J.-I. 2006, Advances in Space Research, 38, 1968

Kenyon, S. J., & Bromley, B. C. 2012, AJ, 143, 63

Kouchi, A., Yamamoto, T., Kozasa, T., Kuroda, T., & Greenberg, J. M. 1994, A&A, 290, 1009

Koyama, Y., Kodama, T., Tadaki, K.-i., et al. 2014, ApJ, 789, 18

Lacerda, P., & Jewitt, D. C. 2007, AJ, 133, 1393

Lellouch, E., Kiss, C., Santos-Sanz, P., et al. 2010, A&A, 518, L147

Leto, G., & Baratta, G. A. 2003, A&A, 397, 7

Leto, G., Gomis, O., & Strazzulla, G. 2005, Memorie della Societa Astronomica Italiana Supplementi, 6, 57

Levison, H. F., & Morbidelli, A. 2003, Nature, 426, 419

Levison, H. F., Morbidelli, A., Van Laerhoven, C., Gomes, R., & Tsiganis, K. 2008, Icarus, 196, 258

Licandro, J., Pinilla-Alonso, N., Pedani, M., et al. 2006, A&A, 445, L35

Lim, T. L., Stansberry, J., Müller, T. G., et al. 2010, A&A, 518, L148

Lockwood, A. C., Brown, M. E., & Stansberry, J. 2014, Earth Moon and Planets, 111, 127

Lord, S. D., 1992, NASA Technical Memorandum 103957

Mastrapa, R. M. E., & Brown, R. H. 2006, Icarus, 183, 207

Mastrapa, R. M., Bernstein, M. P., Sandford, S. A., et al. 2008, Icarus, 197, 307

Mastrapa, R. M. E., Grundy, W. M., & Gudipati, M. S. 2013, The Science of Solar System Ices, 371

McKinnon, W. B., Prialnik, D., Stern, S. A., & Coradini, A. 2008, The Solar System Beyond Neptune, 213

Merk, R., & Prialnik, D. 2006, Icarus, 183, 283

Merlin, F., Guilbert, A., Dumas, C., et al. 2007, A&A, 466, 1185

Merlin, F., Alvarez-Candal, A., Delsanti, A., et al. 2009, AJ, 137, 315

Newman, S. F., Buratti, B. J., Brown, R. H., et al. 2008, Icarus, 193, 397

Owen, T. C., Roush, T. L., Cruikshank, D. P., et al. 1993, Science, 261, 745

Pearl, J., Ngoh, M., Ospina, M., & Khanna, R. 1991, J. Geophys. Res., 96, 477

Porco, C. C., Helfenstein, P., Thomas, P. C., et al. 2006, Science, 311, 1393

Porter, S. B., Desch, S. J., & Cook, J. C. 2010, Icarus, 208, 492

Prialnik, D., & Podolak, M. 1995, Icarus, 117, 420

Quirico, E., & Schmitt, B. 1997, Icarus, 127, 354

Rabinowitz, D. L., Barkume, K., Brown, M. E., et al. 2006, ApJ, 639, 1238

Roth, L., Saur, J., Retherford, K. D., et al. 2014, Science, 343, 171

Ruiz, J., & Tejero, R. 2000, J. Geophys. Res., 105, 29283

Santos-Sanz, P., Lellouch, E., Fornasier, S., et al. 2012, A&A, 541, A92

Schaller, E. L., & Brown, M. E. 2007, ApJ, 670, L49

Smith, B. A., Soderblom, L. A., Banfield, D., et al. 1989, Science, 246, 1422

Spencer, J. R., Barr, A. C., Esposito, L. W., et al. 2009, Saturn from Cassini-Huygens, 683

Stansberry, J., Grundy, W., Brown, M., et al. 2008, The Solar System Beyond Neptune, 161

Suzuki, R., Tokoku, C., Ichikawa, T., et al. 2008, PASJ, 60, 1347

Tanaka, I., Breuck, C. D., Kurk, J. D., et al. 2011, PASJ, 63, 415

Taffin, C., Grasset, O., Le Menn, E., et al. 2012, Planet. Space Sci., 61, 124

Trujillo, C. A., Brown, M. E., Barkume, K. M., Schaller, E. L., & Rabinowitz, D. L. 2007, ApJ, 655, 1172

Trujillo, C. A., Sheppard, S. S., & Schaller, E. L. 2011, ApJ, 730, 105

Verbiscer, A., & Helfenstein, P. 1998, Solar System Ices, 227, 157

Volk, K., & Malhotra, R. 2012, Icarus, 221, 106

Weidenschilling, S. J. 2004, Comets II, 97

Zheng, W., Jewitt, D., & Kaiser, R. I. 2009, Journal of Physical Chemistry A, 113, 11174

This preprint was prepared with the AAS LaTeX macros v5.2.

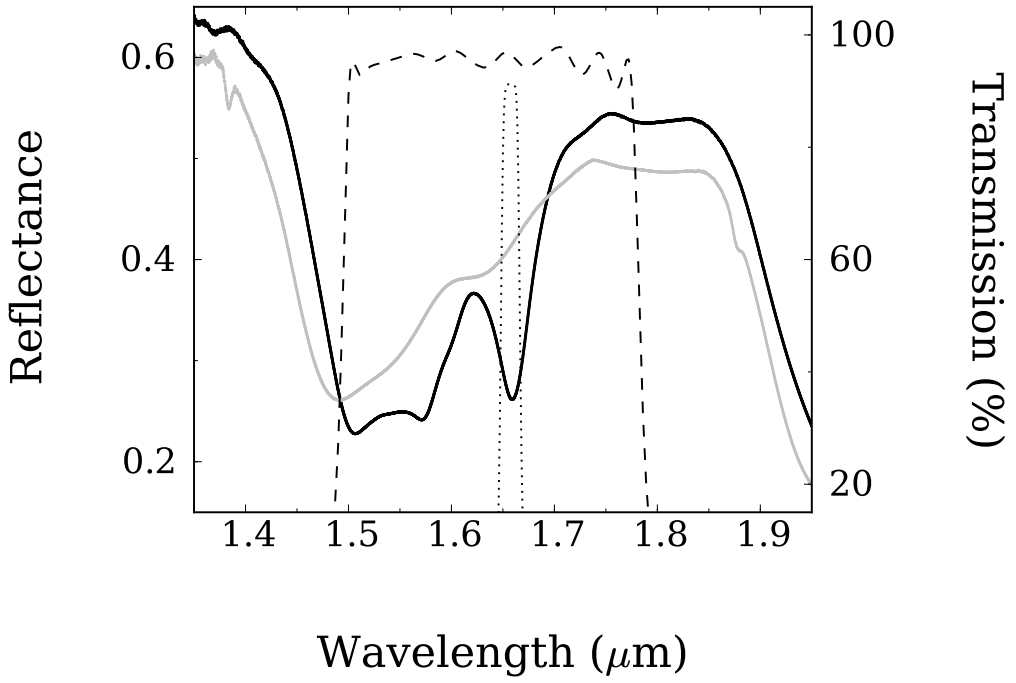

Fig. 1.— Near-infrared reflectance spectra of H_2O ice in crystalline (solid line) and amorphous (gray line) states (from Mastrapa et al. 2008). The dashed and dotted curves show transmission curves of the H-band and NB1657 filters installed in MOIRCS, respectively

Table 1: Orbital elements (semi-major axis, a, eccentricity, e, and inclination, i), absolute visual magnitude ($\mathcal{H}_V$), diameter (D), and spectral parameters (amount of H_2O ice, f_{H_2O} and slope of the continuum, m_{cont}; Brown et al. 2012) of observed objects.

Object	a (au)	e	i (deg)	$\mathcal{H}_V$ (mag)	D (km)	f_{H_2O}	m_{cont}
(38628) Huya	39.41	0.276	15.5	4.9	458 ± 9 [a]	0.08 ± 0.02	-0.09 ± 0.00
(42355) Typhon	38.11	0.540	2.4	7.5	185 ± 7 [b]	0.31 ± 0.17	0.05 ± 0.10
(50000) Quaoar	43.22	0.035	8.0	2.4	1074 ± 38[a]	0.29 ± 0.01	0.07 ± 0.00
(65489) Ceto	101.91	0.825	22.3	6.4	281 ± 11[b]	0.17 ± 0.28	-0.10 ± 0.17
(90482) Orcus	39.44	0.219	20.5	2.2	958 ± 23[a]	0.44 ± 0.01	-0.36 ± 0.03
(136108) Haumea	43.17	0.192	28.2	0.1	$1240\ ^{+69}_{-58}$ [a]	0.66 ± 0.00	-0.40 ± 0.00
(315530) 2008 AP_{129}	42.07	0.143	27.4	4.9	$471\ ^{+161}_{-79}$ [c]	0.14 ± 0.09	0.04 ± 0.05

[a] Fornasier et al. (2013).

[b] Santos-Sanz et al. (2012).

[c] Estimated from $\mathcal{H}_V$ assuming a geometric albedo of 0.09±0.04, the average value of TNOs from Santos-Sanz et al. (2012).

Table 2: Observational circumstances.

Object	UT	Airmass	Seeing[a] (arcsec)	H[b] (sec)	NB1657[c] (sec)
(90482) Orcus	07:28–08:28	1.13–1.19	0.64	880	1260
(315530) 2008 AP_{129}	08:34–09:38	1.20–1.38	0.64	840	1440
(42355) Typhon	10:08–11:12	1.10–1.17	0.75	780	1440
(65489) Ceto	11:53–12:29	1.34–1.46	0.64	500	720
(136108) Haumea	12:34–13:24	1.06–1.16	0.66	600	810
(38628) Huya	13:50–14:53	1.14–1.27	0.76	840	1440
(50000) Quaoar	14:57–15:42	1.22–1.25	0.78	450	1080

[a]Typical full width at half maximum of point sources.

[b]Total exposure time in the H filter.

[c]Total exposure time in the NB1657 filter.

Table 3: Results of Photometry.

Object	H[a] (mag)	$\Delta(H$–NB1657)[a] (mag)
(90482) Orcus	17.89 ± 0.03	-0.045 ± 0.010
(315530) 2008 AP_{129}	19.19 ± 0.03	-0.031 ± 0.024
(42355) Typhon	18.24 ± 0.03	-0.030 ± 0.017
(65489) Ceto	18.85 ± 0.03	+0.033 ± 0.032
(136108) Haumea	16.37 ± 0.03	-0.109 ± 0.011
(38628) Huya	17.57 ± 0.03	-0.016 ± 0.016
(50000) Quaoar	16.74 ± 0.03	-0.040 ± 0.012

[a]The errors show the 1-σ uncertainty.

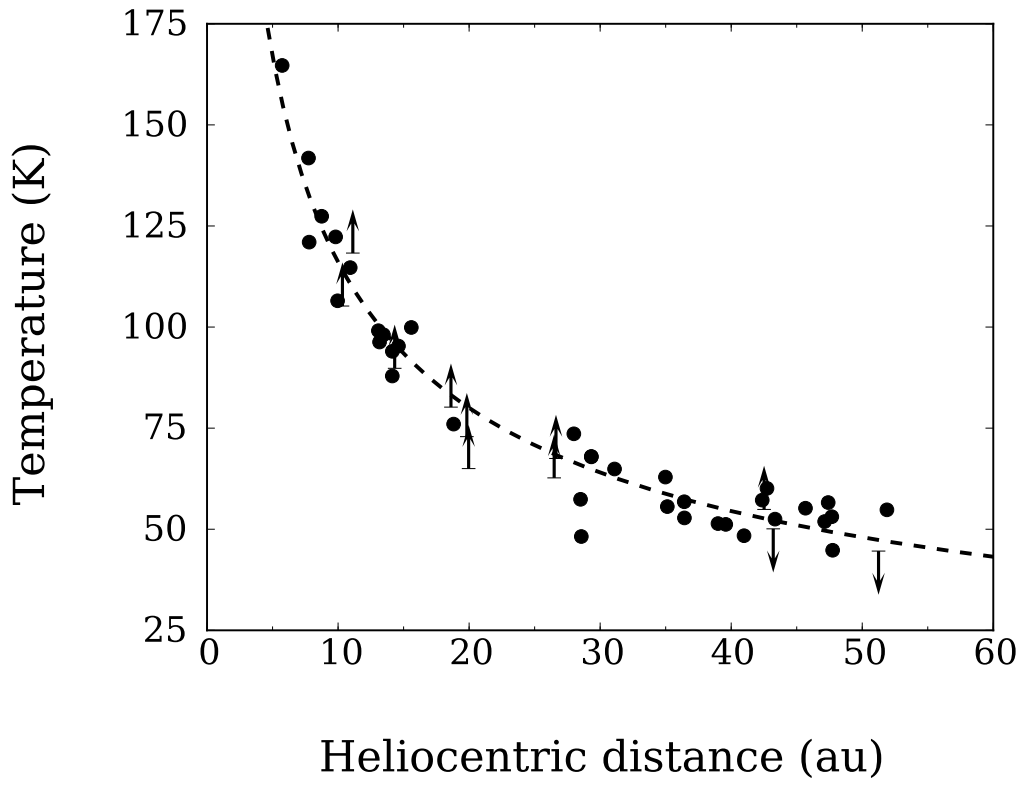

Fig. 2.— Temperatures (T) of TNOs and Centaurs based on Spitzer Space Telescope 24- and 70-μm data (Stansberry et al. 2008) as a function of the heliocentric distance ($r_{\rm h}$). The dashed line shows a best-fit expression of $T \propto r_{\rm h}^{-1/2}$ (see text).

Table 4: Estimated crystallinity factors with grain size of 50 μm in diameter.

Object	$r_{\rm h}$[a] (au)	T[b] (K)	H_2O ice spectra[c]	Crystallinity factor[d]
(90482) Orcus	48.0	49	crys_50K, amorph_low	$0.53^{+0.08}_{-0.09}$
(315530) 2008 AP_{129}	37.9	56	crys_60K, amorph_low	$1.00^{+0.00}_{-0.47}$
(42355) Typhon	19.1	82	crys_80K, amorph_high	$0.79^{+0.21}_{-0.27}$
(136108) Haumea	50.8	48	crys_50K, amorph_low	$0.77^{+0.06}_{-0.05}$
(38628) Huya	28.6	66	crys_70K, amorph_low	$0.93^{+0.07}_{-0.93}$
(50000) Quaoar	43.1	52	crys_50K, amorph_low	$0.82^{+0.15}_{-0.15}$

[a]Heliocentric distance at the observation.

[b]Thermal temperature from Equation (4).

[c]The optical constant dataset derived from laboratory spectra provided by Mastrapa et al. (2008).

[d]The errors show the 1-σ uncertainty.

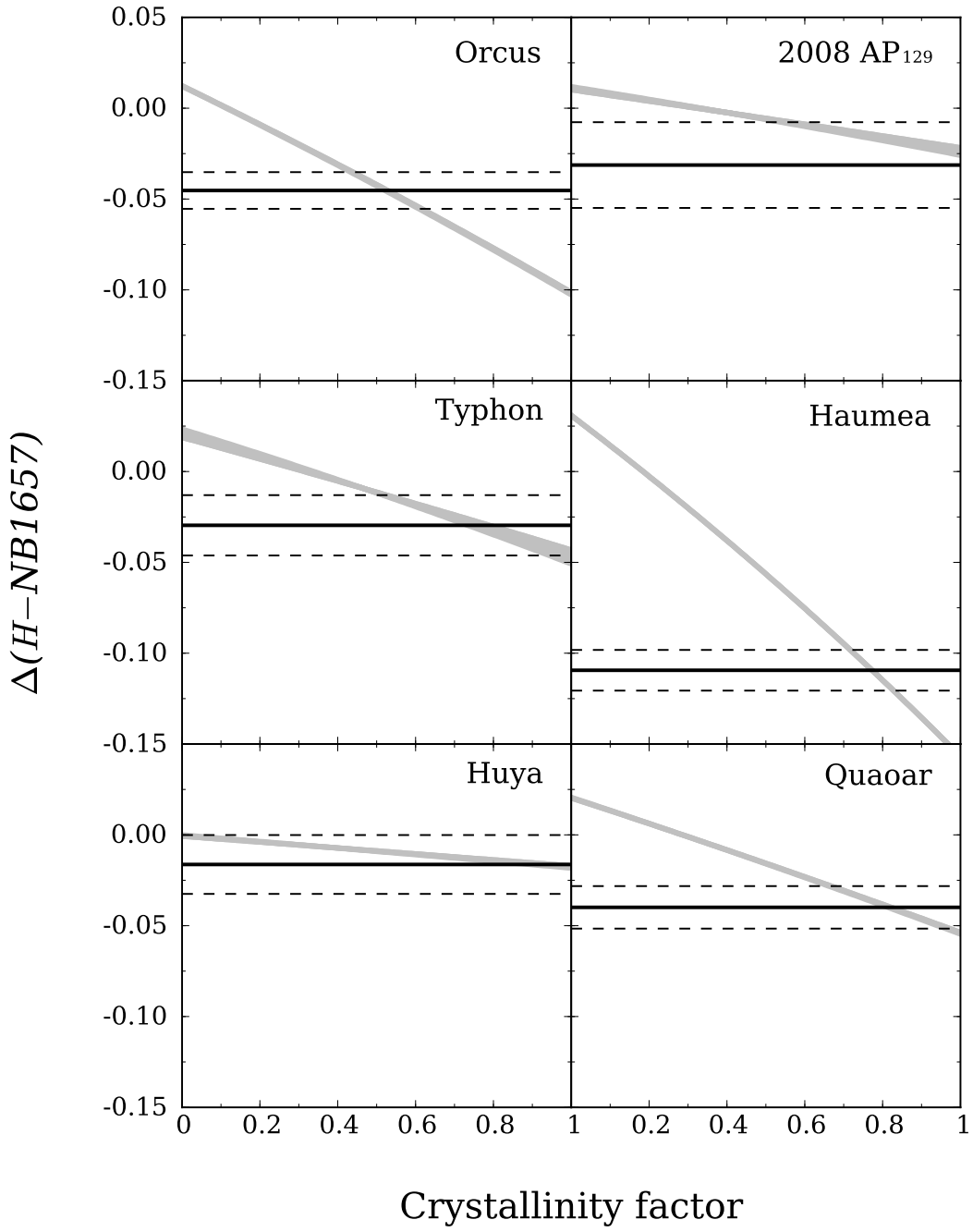

Fig. 3.— Relative $H-$NB1657 indexes of the observed objects (solid lines) and 1 σ errors of photometry (dashed lines). The gray lines show the relation between $H-$NB1657 index and crystallinity factor estimated from the model spectra. The width of gray lines represents uncertainty of the model parameters (see Table 1).

Table 5: Dependency of estimated H_2O ice fraction f_{H_2O} on crystallinity f_{crys} (see text).

	f_{crys}	f_{H_2O}			
Given	1.00	0.70	0.50	0.30	0.10
	0.50	0.69	0.50	0.30	0.10
Best-fit	0.25	0.69	0.49	0.29	0.10
	0.00	0.68	0.48	0.29	0.10

Table 6: Estimated crystallinity factors with lower temperatures.

Object	T^{a} (K)	H_2O ice spectra[b]	Crystallinity factor[c]
(90482) Orcus	42	crys_40K, amorph_low	$0.51^{+0.09}_{-0.08}$
(315530) 2008 AP_{129}	48	crys_50K, amorph_low	$1.00^{+0.00}_{-0.47}$
(42355) Typhon	70	crys_70K, amorph_high	$0.72^{+0.24}_{-0.24}$
(136108) Haumea	41	crys_40K, amorph_low	$0.75^{+0.06}_{-0.05}$
(38628) Huya	56	crys_60K, amorph_low	$0.89^{+0.11}_{-0.89}$
(50000) Quaoar	44	crys_40K, amorph_low	$0.80^{+0.15}_{-0.15}$

[a]Reduced thermal temperature (see text).

[b]The optical constant dataset derived from laboratory spectra provided by Mastrapa et al. (2008).

[c]The errors show the 1-σ uncertainty.

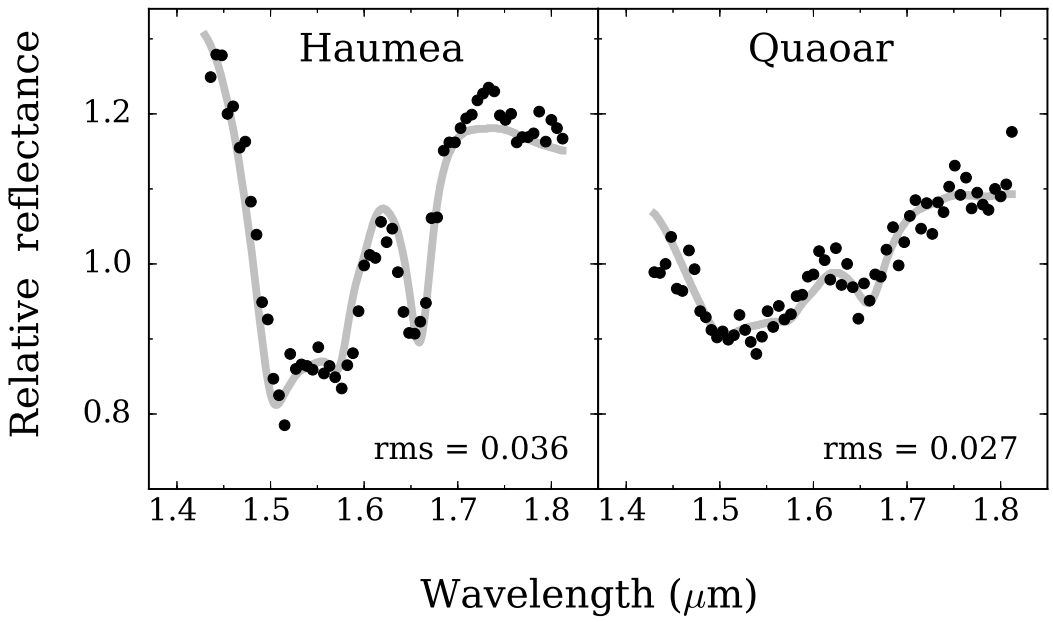

Fig. 4.— Model spectra of Haumea (left) and Quaoar (right) with the determined fractions of crystalline H_2O ice (gray lines). The dots show the published spectral data for comparison.

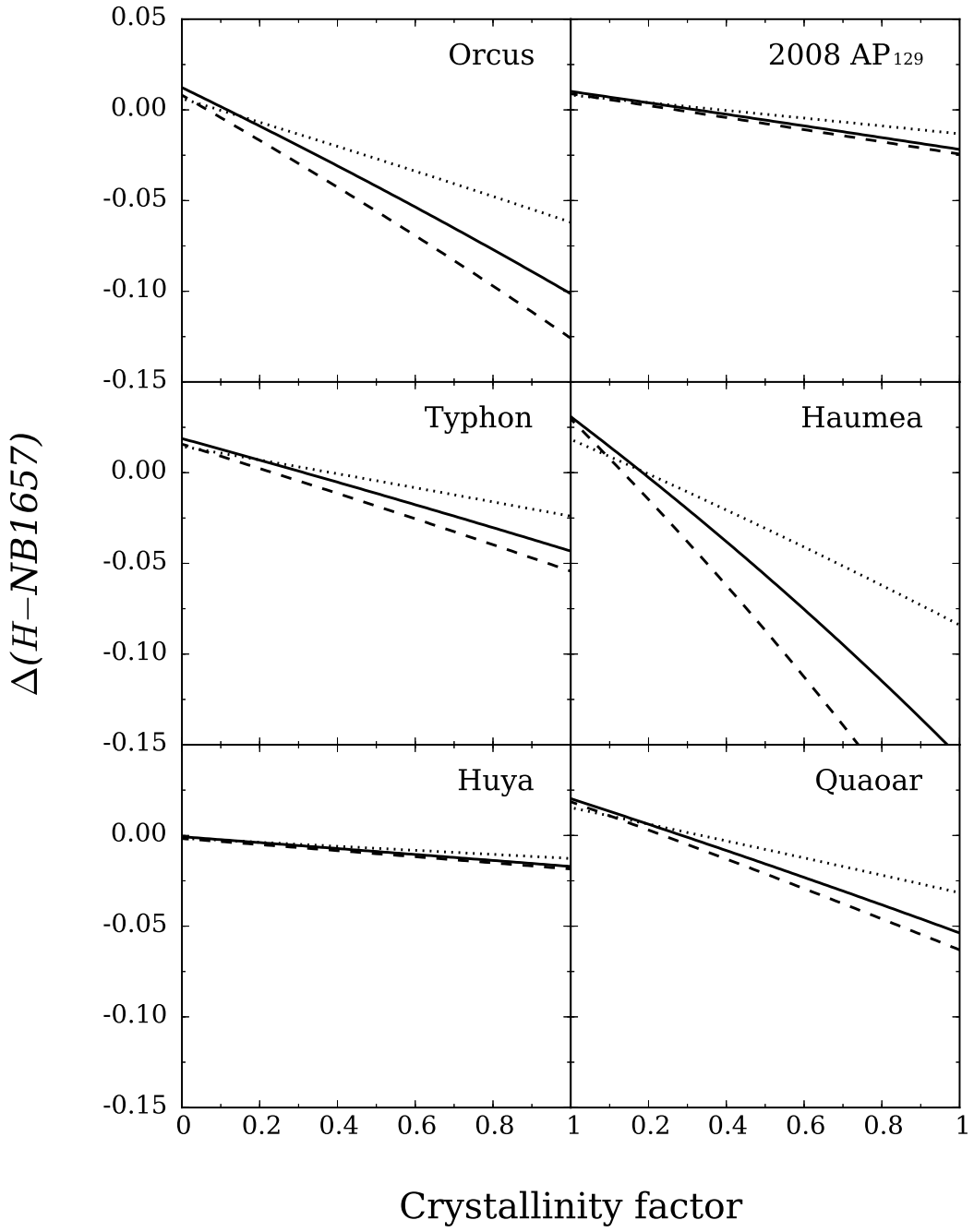

Fig. 5.— The relations between $H-$NB1657 index and crystallinity factor estimated from the model spectra with grain size of 10 μm (dotted lines), 50 μm (solid lines), and 200 μm (dashed lines).

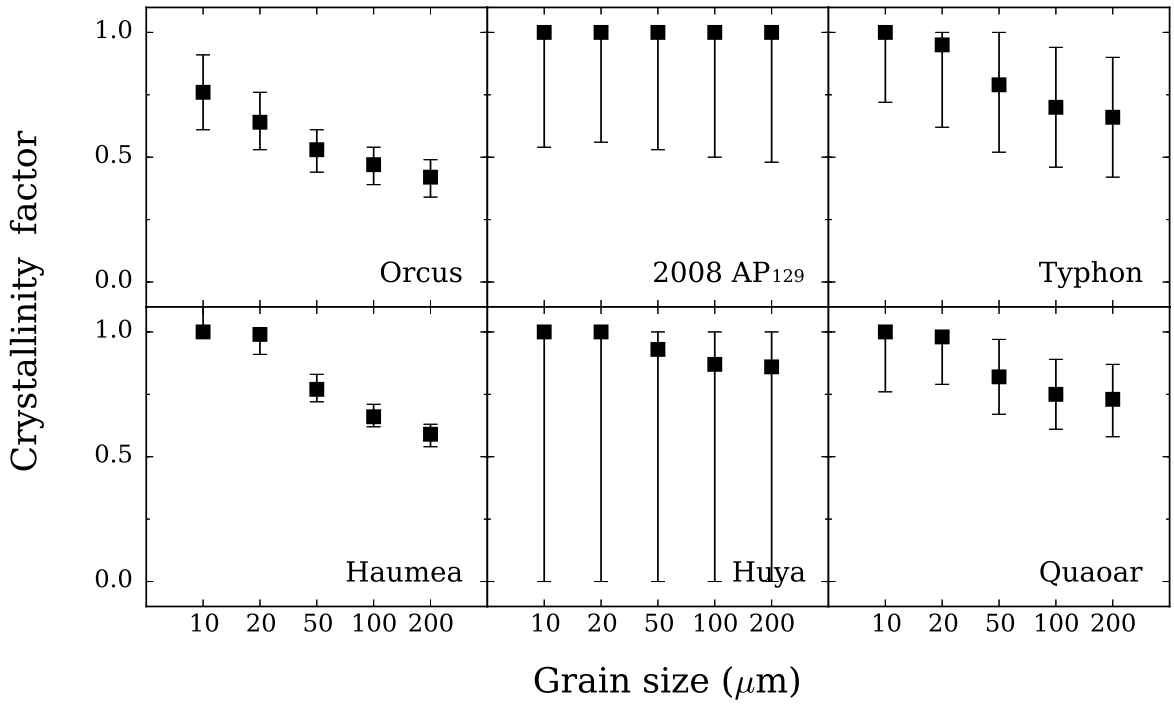

Fig. 6.— Dependency of the obtained crystallinity factors on assumed grain size from 10 μm to 200 μm in diameter. The error bars show the 1-σ uncertainty.

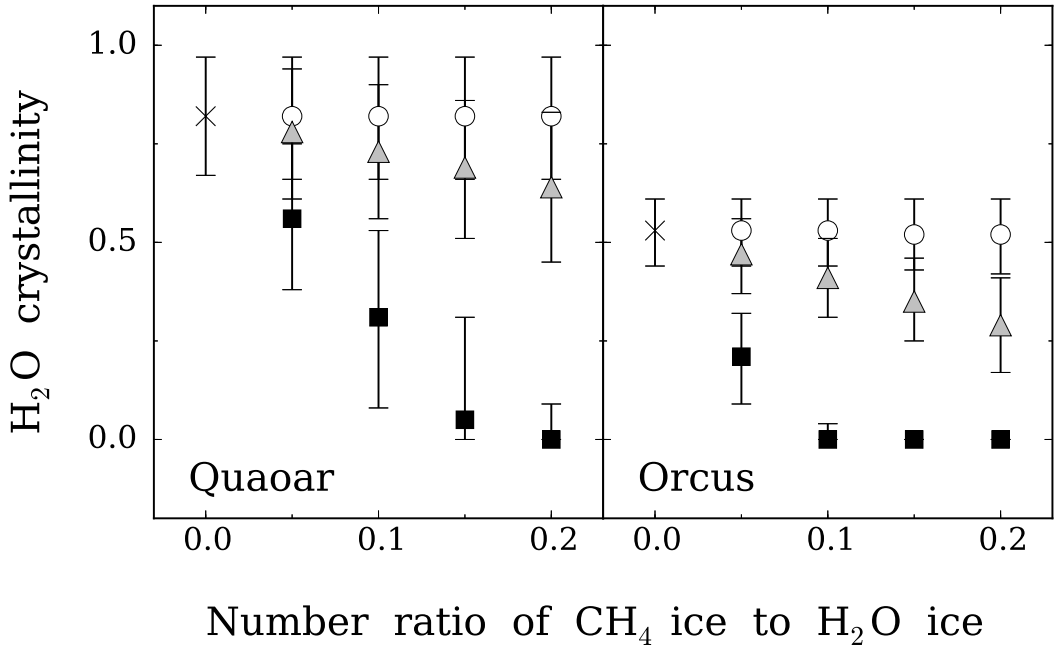

Fig. 7.— Dependency of the obtained crystallinity factors on the particle number ratio of CH_4/H_2O. The grain sizes of CH_4 ice are 10 μm (open circles), 50 μm (triangles), and 100 μm (squares) in diameter. The grain size of H_2O ice is assumed to be 50 μm in diameter. The crosses show the case of absence of CH_4 ice. The error bars show the 1-σ uncertainty.